



## City Research Online

### City, University of London Institutional Repository

---

**Citation:** Gkantou, M., Georgantzia, E., Kadhim, A., Kamaris, G. S. & Sadique, M. (2023). Geopolymer concrete-filled aluminium alloy tubular cross-sections. *Structures*, 51, pp. 528-543. doi: 10.1016/j.istruc.2023.02.117

This is the published version of the paper.

This version of the publication may differ from the final published version.

---

**Permanent repository link:** <https://openaccess.city.ac.uk/id/eprint/34171/>

**Link to published version:** <https://doi.org/10.1016/j.istruc.2023.02.117>

**Copyright:** City Research Online aims to make research outputs of City, University of London available to a wider audience. Copyright and Moral Rights remain with the author(s) and/or copyright holders. URLs from City Research Online may be freely distributed and linked to.

**Reuse:** Copies of full items can be used for personal research or study, educational, or not-for-profit purposes without prior permission or charge. Provided that the authors, title and full bibliographic details are credited, a hyperlink and/or URL is given for the original metadata page and the content is not changed in any way.

---

---

---

City Research Online:

<http://openaccess.city.ac.uk/>

[publications@city.ac.uk](mailto:publications@city.ac.uk)

---



# Geopolymer concrete-filled aluminium alloy tubular cross-sections

Michaela Gkantou<sup>a,\*</sup>, Evangelia Georgantzia<sup>a</sup>, Abdullah Kadhim<sup>b</sup>, George S. Kamaris<sup>a</sup>,  
Monower Sadique<sup>a</sup>

<sup>a</sup> School of Civil Engineering and Built Environment, Liverpool John Moores University, United Kingdom

<sup>b</sup> Department of Building and Construction Technologies Engineering, Al-Mustaqbal University College, Iraq

## ARTICLE INFO

### Keywords:

Aluminium alloy  
Geopolymer concrete  
Stub columns  
Beams  
Composite structures  
European codes

## ABSTRACT

Composite steel–concrete members are adopted in structural applications as a cost-effective and high-speed construction practice. Exploiting the superior corrosion and strength-to-weight properties of structural aluminium, research on composite aluminium–concrete members has been reported. Aiming for an even more sustainable and durable structural member, this paper proposes combining structural aluminium alloys with low carbon geopolymer concrete (GC) to form a structural member with lower environmental footprint. To this end, an experimental programme on geopolymer concrete-filled aluminium alloy tubular (GCFAT) cross-sections is performed. A total of 24 tests on stub columns and 12 tests on beams were carried out. In particular, 4 square hollow sections infilled with one-part geopolymer concrete were tested under uniform compression and under uniaxial bending. The hollow sections were fabricated from 6082-T6 heat-treated aluminium alloy. The same cross-sections were also tested as bare and infilled with ordinary Portland cement (OPC) concrete for comparison purposes. It is shown that the strength of the composite sections is significantly increased compared to the bare ones. In particular, the average strength increase was in the range of 16.5%–93.3% and of 23%–93.1% for GC and OPC-aluminium stub columns, respectively. In beams, the strength increase was in the range of 14.1%–53.6% for GC-aluminium and of 10.2%–48.9% for OPC-aluminium specimens. In absence of codified design rules for geopolymer concrete–aluminium structures, design formulae based on the European standards for composite steel–concrete members, with the material properties of steel and concrete replaced by those of aluminium alloy and GC, respectively, are adopted. The obtained results demonstrated that the proposed design methodology is suitable for the design of GCFAT cross-sections and beams, providing reasonably accurate and consistent strength predictions. Overall, the potential of geopolymer concrete-filled aluminium tubular cross-sections as a novel cement-free, sustainable, and structurally efficient composite cross-section is demonstrated.

## 1. Introduction

### 1.1. Composite structures

Over the past few decades, composite construction is fast becoming a key application in high performance engineering structures. Concrete-filled steel tubular (CFST) members have been efficiently employed as compression members combining the advantageous properties of both materials, i.e., steel and concrete. In particular, the concrete infill delays local buckling by bracing the steel tube to resist the developed deformations and thus achieving higher stiffness, ductility and compression resistance [1–6]. Therefore, the robust mechanical properties of the CFST columns allow for employment of smaller cross-sectional sizes for given loads leading to increased net floor space [4,7–8]. This, coupled

with the lower need for external formwork in the concreting process [9–11], demonstrates the potential of the CFST column concept to reduce the construction time and costs.

In structural applications where the structure's self-weight and resistance against corrosion are primary design concerns, it could be more suitable to replace the steel tubes with aluminium alloy ones. Aluminium alloys as a structural material are lightweight, as their density is significantly lower (approximately 2.5 times) compared to steel. Moreover, they have excellent corrosion resistance and thereby are suitable for structural applications in marine and offshore environments. Similar to CFST columns, the concrete-filled aluminium tubular (CFAT) columns can take advantages from both materials, i.e., aluminium alloy and concrete, denoting improved structural performance.

\* Corresponding author.

E-mail address: [m.gkantou@ljmu.ac.uk](mailto:m.gkantou@ljmu.ac.uk) (M. Gkantou).

<https://doi.org/10.1016/j.istruc.2023.02.117>

Received 14 February 2023; Accepted 25 February 2023

Available online 21 March 2023

2352-0124/© 2023 The Author(s). Published by Elsevier Ltd on behalf of Institution of Structural Engineers. This is an open access article under the CC BY license (<http://creativecommons.org/licenses/by/4.0/>).

To date, the reported research work on the structural response of CFAT columns is relatively limited [12]. Zhou & Young [13] performed axial compression tests on concrete-filled aluminium stub columns with square hollow sections (SHSs) and rectangular hollow sections (RHSs) [14,15]. Later, Zhou & Young [16,17] extended their experimental investigation on circular hollow sections and suggested design criteria considering the observed material interaction. Following, Zhou & Young [18] assessed experimentally the compressive response of concrete-filled double-skin tubes and proposed design formulae for their ultimate capacity. In a more recent study, Wang et al. [19] utilised the data reported by Zhou & Young [16] to evaluate whether the “nominal yield strength” method adopted by GB 50936 [20] for CFST is applicable to CFAT. Further to stub columns, the potential of composite aluminium-concrete members [21–23] has also been demonstrated. Feng et al. [24] performed bending tests on CFAT rectangular and square sections and assessed the applicability of current design rules for concrete-steel members to concrete-aluminium members, whereas Chen et al. [25] experimentally investigated the flexural behaviour of CFAT beams strengthened by carbon fibre-reinforced polymer layers.

### 1.2. Geopolymer concrete

In the above studies of CFAT members, the aluminium tubes were infilled with concrete produced by ordinary Portland cement (OPC). As known, the production of OPC is a highly energy consuming process releasing almost 10% of the total worldwide carbon dioxide CO<sub>2</sub> emissions [26]. Recent studies have shown that geopolymers or alkali-activated cements could be used as a potential alternative to OPC, denoting sufficiently high mechanical properties, whilst delivering an 80% reduction in CO<sub>2</sub> emissions [27,28]. Geopolymers are usually composed of two main parts: (i) an aluminosilicate precursor (Al<sub>2</sub>O<sub>3</sub>-SiO<sub>2</sub>) and (ii) a source of alkaline and activation agent. The latter are often based on chemical and high purity substances, such as sodium hydroxides/silicates, and could inhibit the wide-spread construction applications of geopolymers due to their high carbon impact, hazardous effect, and cost criteria [29–31]. Therefore, recent research trends have focused on the development of one-part alkali activated geopolymer cement (AAC), where the alkali activators are supplied in the form of solid powder based on the use of waste materials [32,33]. Like traditional cement and cement-based materials, in one-part AAC, only water is needed and their long-term performance was also reported [34].

Research on the mechanical properties of geopolymer concrete (GC) was reported in [35], demonstrating superior performance of GC compared to conventional OPC concrete. The increase in strength was attributed to the denser interfacial zone created between the aggregates and the geopolymer paste [35]. In [36], the matrix of geopolymer was found to be denser, and as a result, the elastic modulus to be higher, compared to OPC concrete. The results of another experimental study on GC examined the bond behaviour between concrete and fibre reinforced polymers (FRP) [37]. Investigations on the confinement of GC through the use of steel reinforcement were examined by [38,39]. Corrosion resistance studies were presented in [40–42], denoting enhanced performance of GC compared to OPC, due to the strong and adherent silicate membrane formed by the geopolymerisation process. The structural performance of geopolymer-concrete-filled steel tubular (GCFST) members under concentric compression, pure bending and combined compression and bending was also investigated experimentally and numerically by [43]. The obtained data were used to assess the applicability of the existing design codes for composite steel-concrete structures. It was concluded that the existing criteria could be applied for the design of composite steel-geopolymer concrete structures providing safe strength predictions. Katwal et al. [44] recently tested composite stainless steel-geopolymer concrete columns under ambient and fire conditions and found that the fire resistance significantly improves by GC. Finally, Zhou et al. [45] suggested a new type of assembled GCFST columns frame with controllable deformation connected GC

walls, whilst Ahmad et al. [46] proposed a novel glass fiber reinforced polymer (GFRP) bar reinforced GC filled GFRP tubular column.

### 1.3. Research significance

- (i) The present study aims to combine the benefits of composite aluminium structures and geopolymer concrete, by proposing a new composite structural member, i.e., geopolymer concrete-filled aluminium alloy tubular (GCFAT) cross-section and examining its structural performance. This new structural member will allow exploitation of the superior properties of structural aluminium alloys [47] (i.e., corrosion resistance, strength-to-weight ratio, recyclability) and of geopolymer concrete (i.e., mechanical properties, low carbon footprint) in a combined manner, leading to a structurally efficient, sustainable and durable member.
- (ii) Based on European design guidelines for composite steel-concrete and for aluminium structures [48,49], the study utilises the experimentally obtained data to propose design formulae for strength predictions of the proposed composite cross-section.
- (iii) In addition, the study generates data for the performance of GC in structural applications, which are currently scarce. In particular, the possibility of using any form of GC in structural applications has not been vindicated in the UK. Due to non-availability of real site case studies or performance data of GC in structural applications, designers are reluctant to specify this material. Through experimental studies like the one presented herein, it is expected that the acceptance of GC by construction industry, designers and workers will be improved. Note that the dimensions of the cross-sections presented herein are available in current aluminium industry and are similar to those researched in past studies for aluminium-concrete members [21–23].
- (iv) Finally, as mentioned in Section 1.1, research on aluminium-OPC concrete members has already been reported. However, it is known that aluminium reacts with the alkalis found in OPC concrete [50] and a coating is recommended in aluminium structures to protect them from corrosion, when they come in contact with OPC concrete. When OPC concrete is replaced with GC, the need for this coating may be eliminated, due to the full consumption of alkali cations (Ca<sup>+2</sup>, Na<sup>+1</sup>) by the higher amounts of aluminosilicate compounds blended with the alkaline activators during the geopolymerisation mechanism. The elimination of coating in aluminium could be a significant advantage of the proposed composite section and even though the corrosion performance of the composite GC-aluminium member is not examined herein, investigations in this field are encouraged for future work, as also mentioned in Section 6.

## 2. Experimental programme

This article reports and discusses experimental data of a total of 24 compression tests and 12 beam tests. For comparison purposes, the same cross-sections were tested as bare and infilled with OPC concrete and geopolymer concrete. The considered hollow sections were made of 6082-T6 heat treated aluminium alloy.

### 2.1. Test specimens

Four different SHSs made of 6082-T6 heat-treated aluminium alloy were examined in the present study. The sections were fabricated with the extrusion process. All cross-sections had nominal outer depth  $D$  and width  $B$  of 50.8 mm. Four nominal thicknesses  $t$ , namely 1.6, 2.7, 3.3 and 4.8 mm, were considered, enabling to investigate the cross-sectional response in a broad range of width-to-thickness ratio  $B/t$  values (see Table 1 for stub columns and Table 2 for beams). Following the technical memorandum for stub column tests [51], the specimens were cut in

**Table 1**  
Mean measured dimensions of tested stub columns.

Specimen	D (mm)	B (mm)	t (mm)	B/t	L (mm)
<i>BAT specimens</i>					
50.8 × 50.8 × 1.6-a	51.04	50.80	1.62	31.36	153.00
50.8 × 50.8 × 1.6-b	50.89	50.36	1.64	30.71	152.90
50.8 × 50.8 × 2.7-a	50.86	50.82	2.68	18.96	153.00
50.8 × 50.8 × 2.7-b	50.78	50.10	2.71	18.49	153.00
50.8 × 50.8 × 3.3-a	51.32	50.70	3.27	15.50	153.00
50.8 × 50.8 × 3.3-b	51.49	51.20	3.25	15.75	152.90
50.8 × 50.8 × 4.8-a	51.22	51.00	4.79	10.65	153.00
50.8 × 50.8 × 4.8-b	51.06	50.79	4.73	10.74	153.00
<i>GCFAT specimens</i>					
50.8 × 50.8 × 1.6-GC-a	50.96	50.23	1.61	31.20	152.90
50.8 × 50.8 × 1.6-GC-b	50.97	50.92	1.61	31.63	152.90
50.8 × 50.8 × 2.7-GC-a	50.87	50.31	2.56	19.65	152.90
50.8 × 50.8 × 2.7-GC-b	50.87	50.48	2.62	19.27	152.90
50.8 × 50.8 × 3.3-GC-a	51.02	51.00	3.18	16.04	152.90
50.8 × 50.8 × 3.3-GC-b	51.36	51.35	3.16	16.25	152.90
50.8 × 50.8 × 4.8-GC-a	51.48	50.99	4.73	10.78	152.90
50.8 × 50.8 × 4.8-GC-b	51.08	50.21	4.84	10.37	152.90
<i>CFAT specimens</i>					
50.8 × 50.8 × 1.6-C-a	50.92	50.44	1.69	29.85	152.90
50.8 × 50.8 × 1.6-C-b	50.66	50.55	1.66	30.45	152.90
50.8 × 50.8 × 2.7-C-a	51.13	51.00	2.65	19.25	152.90
50.8 × 50.8 × 2.7-C-b	51.11	50.28	2.59	19.41	152.90
50.8 × 50.8 × 3.3-C-a	50.89	50.63	3.33	15.20	152.90
50.8 × 50.8 × 3.3-C-b	50.33	50.29	3.36	14.97	152.90
50.8 × 50.8 × 4.8-C-a	51.36	50.89	4.78	10.65	152.90
50.8 × 50.8 × 4.8-C-b	51.47	51.32	4.80	10.69	152.90

**Table 2**  
Mean measured dimensions of the tested beams.

Specimen	B/t	D (mm)	B (mm)	t (mm)	L (mm)
	nominal	measured			
<i>BAT beams</i>					
50.8 × 50.8 × 1.6	31.8	51.02	50.70	1.60	599.05
50.8 × 50.8 × 2.7	18.8	51.02	50.70	2.64	599.06
50.8 × 50.8 × 3.3	15.4	50.64	50.60	3.25	599.07
50.8 × 50.8 × 4.8	10.6	50.63	50.60	4.75	599.05
<i>GCFAT beams</i>					
50.8 × 50.8 × 1.6-GC	31.8	50.96	50.63	1.61	599.05
50.8 × 50.8 × 2.7-GC	18.8	50.82	50.76	2.56	599.05
50.8 × 50.8 × 3.3-GC	15.4	50.81	50.73	3.18	599.05
50.8 × 50.8 × 4.8-GC	10.6	51.01	50.81	4.73	599.05
<i>CFAT beams</i>					
50.8 × 50.8 × 1.6-C	31.8	50.88	50.65	1.60	599.08
50.8 × 50.8 × 2.7-C	18.8	50.79	50.79	2.63	599.05
50.8 × 50.8 × 3.3-C	15.4	50.96	50.84	3.22	599.05
50.8 × 50.8 × 4.8-C	10.6	50.86	50.82	4.81	599.05

nominal length  $L$  equal to three times the maximum cross-sectional dimension. In beams, each cross-section was cut from the same tube and had nominal length  $L$  of 600 mm. The specimens were infilled with GC or OPC concrete. The same cross-sections were also tested without infill for comparison purposes. These sections are referred to as bare aluminium tubular (BAT) sections. Each stub column test was executed twice, resulting in a total of 24 stub column tests.

Tables 1 and 2 present the measured dimensions for all the investigated specimens using the nomenclature depicted in Fig. 1. The specimens were designated according to their nominal geometric dimensions and the presence of the GC or OPC concrete infill. In Table 1 for stub column tests, the designation was also followed by the letter “a” or “b” to distinguish the specimens employed in the first and second test, respectively. For instance, the label “50.8 × 50.8 × 3.3-GC-a” defines a stub column specimen with outer depth  $D = 50.8$  mm, outer width  $B = 50.8$  mm and thickness  $t = 3.3$  mm, whilst the letters “GC” indicate that the specimen is infilled with geopolymer concrete. Letter “a” signifies that this specimen was tested first.

2.2. Aluminium 6082-T6: tensile coupon tests

Following the procedure outlined in EN ISO 6892-1 [52], material tensile coupon tests were performed to determine the engineering stress–strain ( $\sigma$ - $\epsilon$ ) response of the examined 6082-T6 heat-treated aluminium alloy. For each investigated SHS, two flat coupons, one from the mid-width of the web and one of the mid-width of the flange, were cut with a nominal width of 12 mm and gauge length of 100 mm. A 50 kN Tinius Olsen testing machine was used to execute the tensile tests applying loading in a 0.2 mm/min displacement rate up to fracture. During testing, the longitudinal strains were recorded through a calibrated extensometer attached onto the mid-length of the coupon, as shown in Fig. 2(a). All fractured coupons are illustrated in Fig. 2(b).

A summary of the obtained test results is reported in Table 3, where  $E$  is the initial modulus of elasticity,  $\sigma_{0.1}$  is the 0.1 % proof stress,  $\sigma_{0.2}$  is the 0.2 % proof stress,  $\sigma_u$  is the ultimate tensile stress,  $\epsilon_f$  is the strain at fracture and  $n$  is the strain hardening exponent based on the material model proposed by Ramberg and Osgood [53] and modified by Hill [54]. Fig. 3 depicts the engineering stress–strain ( $\sigma$ - $\epsilon$ ) response for all cross-sections obtained from the tensile coupon tests. As can be observed, the examined 6082-T6 aluminium alloy exhibits a round stress–strain behaviour without a distinct yield point due to continuous strain hardening. The strain hardening ratio  $\sigma_u/\sigma_{0.2}$  for each examined cross-section is also included in Table 3, reaching up to 109%. Note also that the Poisson’s ratio of the tested aluminium tube is equal to 0.33 [21–23].

2.3. OPC concrete and geopolymer concrete mix

The concrete mix was produced using OPC, medium-coarse sand, coarse aggregate with a maximum size of 10 mm and freshwater with a mix ratio of 1:1.46:2.49:0.53 by weight. In order to determine the maximum compressive strength of the concrete infill, four (100 × 100 × 100) mm<sup>3</sup> standard concrete cubes were cast from the same concrete

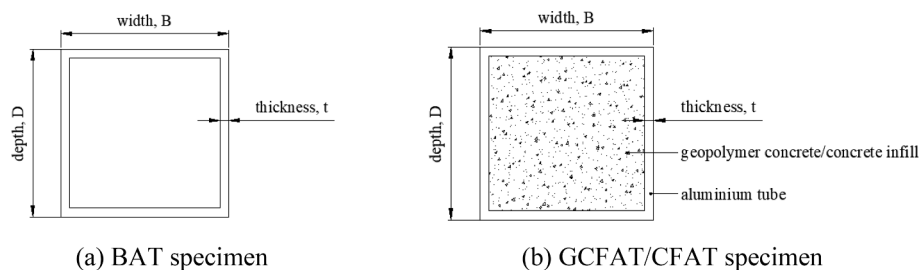


Fig. 1. Geometric properties of the cross sections of the specimens.

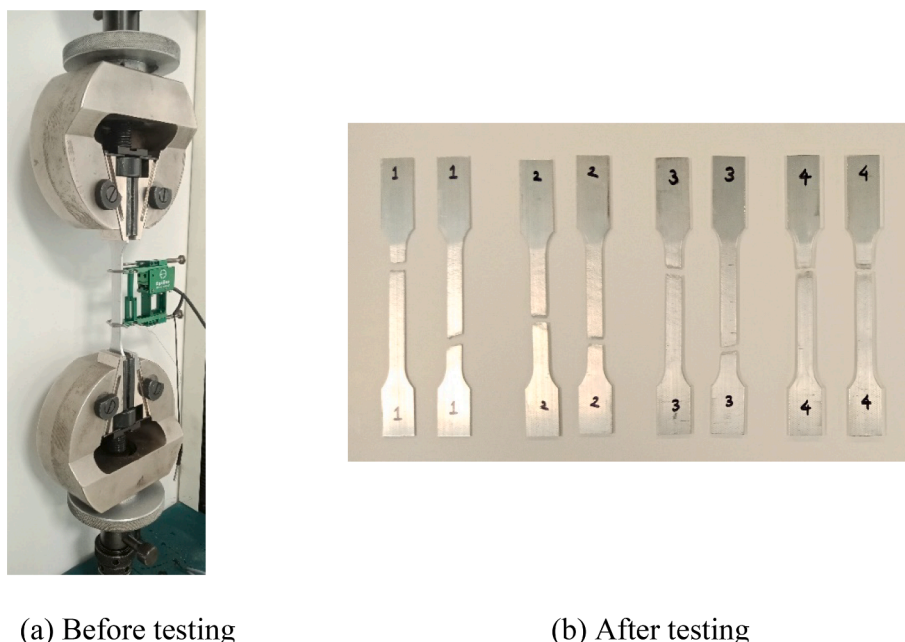


Fig. 2. Tensile coupons.

Table 3  
Material properties obtained from the tensile coupon tests.

Cross-section	$E$ (MPa)	$\sigma_{0.1}$ (MPa)	$\sigma_{0.2}$ (MPa)	$\sigma_u$ (MPa)	$\epsilon_u$ (mm/mm)	$\epsilon_f$ (mm/mm)	$n$	$\sigma_{0.2}/\sigma_{0.1}$
50.8 × 50.8 × 1.6	65,000	283.4	289.1	315.0	0.08	0.11	34.8	1.09
50.8 × 50.8 × 2.7	72,200	329.7	337.1	352.0	0.07	0.10	31.2	1.04
50.8 × 50.8 × 3.3	71,700	295.5	302.2	330.0	0.08	0.09	30.9	1.09
50.8 × 50.8 × 4.8	67,500	299.8	305.9	325.0	0.09	0.16	34.4	1.06

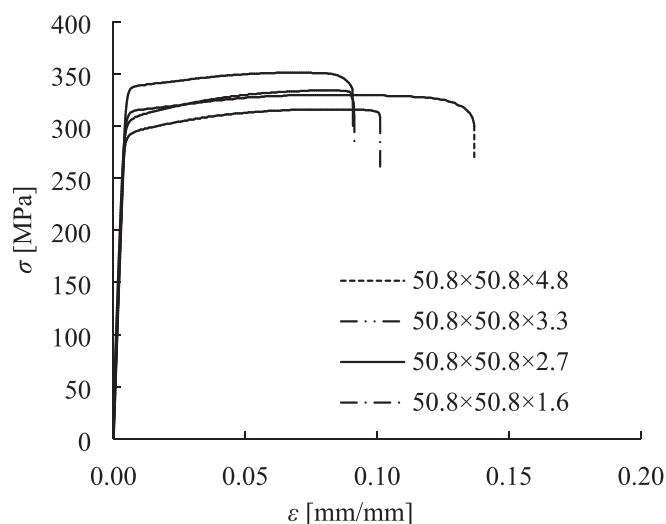


Fig. 3. Stress–strain curves obtained from the tensile coupon tests.

mix used to fill the aluminium tubes of the CFAT stub columns. After casting, the cubes were kept in rest period for 24 h. Following, the cubes were demoulded and were placed in a water tank at ambient temperature for curing. Upon 28 days of curing, the concrete cubes were subjected to axial compression resulting in average compressive cube strength of 37.55 MPa. This concrete mix was used to fill the aluminium tubes of the CFAT specimens, which were left to cure for 28 days before the execution of the stub column and beam tests (Sections 2.4 and 2.5).

The one-part geopolymer powder was developed by blending

metakaolin; originated from natural clay and natural pozzolan, obtained from volcanic tuff sources, as a source of aluminosilicate precursors ( $Al_2O_3-SiO_2$ ). These materials were used to replace the traditional raw materials of GC, such as fly ash and GGBS [55,56]. The alkaline activator was supplied as a waste material from the quicklime production, thus providing the required CaO with high alkalinity, whilst avoiding the hazardous aspects of the synthetic chemicals, such as NaOH and  $Na_2SiO_3$  [30]. The oxide compositions determined by X-Ray fluorescence (XRF) of the developed geopolymer powder and the OPC binder are shown for reference in Table 4. It can be observed that compared to OPC, the geopolymer powder has higher content of alumina, which are required for the alkali-activation process.

The X-Ray diffractions (XRD) of anhydrous GC powder and its hardened paste after 28 days of curing are presented for reference in Fig. 4. The major geopolymerisation products are composed of CaO- $Al_2O_3$ -MgO- $SiO_2$  compounds. The utilisation of a dry alkaline (CaO) activator in the mix transforms the crystallinity diffraction patterns into

Table 4  
The chemical composition of GC and OPC mix.

Chemical composition (Wt.%)	Material (anhydrous)	
	OPC	GC
SiO <sub>2</sub>	26.60	39.80
Al <sub>2</sub> O <sub>3</sub>	2.20	18.23
Fe <sub>2</sub> O <sub>3</sub>	2.43	2.30
CaO	64.11	28.80
Na <sub>2</sub> O	0.27	1.50
K <sub>2</sub> O	0.65	2.39
MgO	1.50	5.80
TiO <sub>2</sub>	1.50	0.80
P <sub>2</sub> O <sub>5</sub>	0.87	–

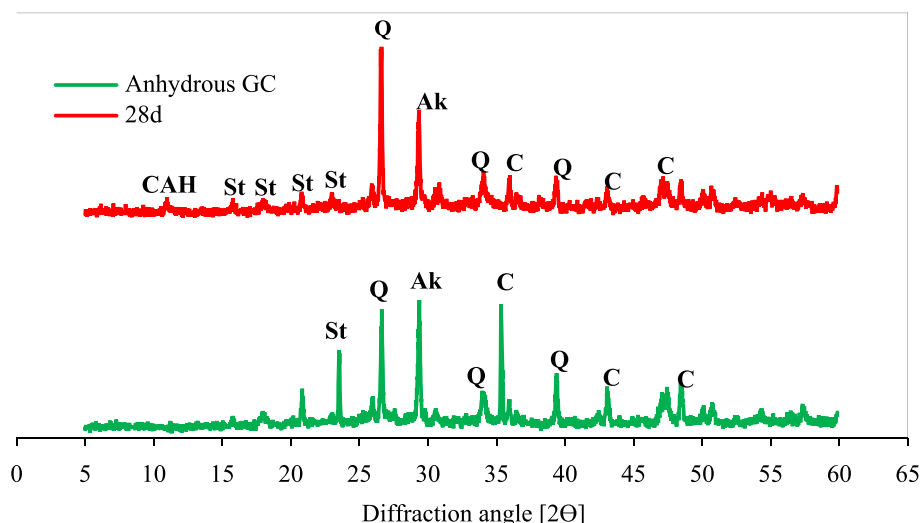


Fig. 4. XRD patterns of anhydrous and hydrated GC paste after 28 days (St: stratlingite, Q: quartz, C: calcite, CAH: calcium aluminate hydrate, Ak: Akermanite).

amorphous patterns and leads to the presence of prevailing vitreous phases. The main phases that are produced are tetra calcium aluminate hydrate (CAH-C<sub>4</sub>AH<sub>13</sub>), calcium alumina silicate hydrates, stratlingite (St - C<sub>2</sub>ASH<sub>8</sub>), quartz and calcite [57–59].

The geopolymer concrete mix was produced using the same mix ratio with that of concrete but using geopolymer powder as sole binder. Similarly, the maximum compressive strength of the geopolymer concrete infill was determined testing four (100 × 100 × 100) mm<sup>3</sup> standard geopolymer concrete cubes cast from the same geopolymer concrete mix used to fill the aluminium tubes of the GCFAT stub columns and beams. After casting, the geopolymer concrete cubes were kept in rest period for 24 h. Then, they were demoulded and following the fabrication procedure proposed in [33], they were placed in a water tank at 50 °C for curing. Curing the geopolymer specimens in a hot water curing regime aimed to enhance the reactivity and the alkali-activation rate of the specimens and to avoid potential problems, such as efflorescence and micro cracking, which could lead to reduction in the compressive strength [33]. Upon 28 days of curing, the cubes were subjected to axial compression resulting in average compressive cube strength of 26.68 MPa. The setting time of the geopolymer mortars were examined according to the British standards 196–3 [60]. The initial and final setting times were recorded to be 87 and 110 min, respectively. Note that the aluminium tubes of GCFAT specimens were filled with geopolymer concrete and were left to cure for 7 days at a water tank of 50 °C and subsequently at ambient environment before the execution of the tests (Sections 2.4 and 2.5). The Poisson’s ratio of the used geopolymer concrete is considered to be in the range of 0.19 – 0.21 according to [61].

The measured compressive strength values of the OPC concrete and GC cubes are summarised in Table 5.

Table 5  
Measured 28 days cube compressive strength of concrete.

OPC concrete (C)		Geopolymer concrete (GC)	
Specimen	<i>f<sub>c,cube</sub></i> (MPa)	Specimen	<i>f<sub>c,cube</sub></i> (MPa)
C-1	33.05	GC-1	25.98
C-2	35.06	GC-2	26.45
C-3	40.44	GC-3	27.15
C-4	41.64	GC-4	27.13
mean	37.55	mean	26.68

### 2.4. Stub column tests

A total of 24 stub column tests were performed aiming to capture their cross-sectional and local buckling response of each considered cross-section. Prior to testing, the top and bottom surfaces of the column specimens were machined flat to ensure uniform distribution of the applied loading [13,17–18]. Moreover, the top infill surface of the GCFAT and CFAT specimens was roughened with a wire brush and then was cast in plaster to fill the longitudinal gap. This practice allowed for simultaneous loading of both infill and aluminium tube. In line with similar studies on composite aluminium stub columns [13,17–18], the BAT/GCFAT/CFAT specimens were also strengthened with carbon FRP strips at both ends to prevent any localised failure.

Fig. 5 shows a schematic illustration of the stub column test arrangement along with the corresponding employed instrumentation. A Mayses servo-controlled hydraulic testing machine with 600 kN capacity was used to execute the stub column tests. The end plates of the testing apparatus were fixed flat and parallel. Alignment of the specimen

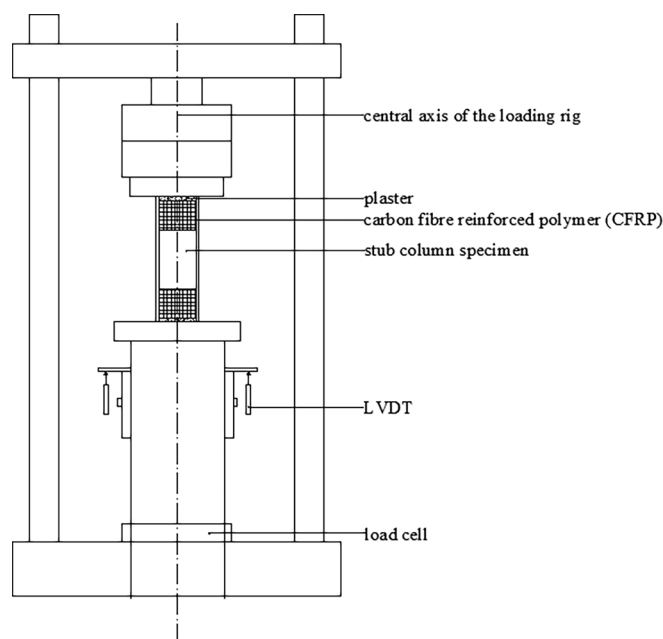


Fig. 5. Schematic illustration of the stub column test arrangement and instrumentation.

was deemed necessary to ensure that the compressive loading is applied concentrically. The compressive loading was applied at 0.2 mm/min displacement rate until failure occurred. Moreover, two linear variable displacement transducers (LVDTs) were placed underneath the bottom end plate of the testing machine to measure the end shortening of the specimen (Fig. 6). A data acquisition system was used to record the applied load and end shortening at 2 s intervals.

### 2.5. Simply supported beam tests

A total of 12 three-point bending tests on simply supported beams were performed aiming to capture their flexural response and quantify the bending moment capacity of each considered cross-section. Three-point bending configuration was adopted allowing to explore the cross-sectional response under moment gradient. Fig. 7 displays a schematic illustration of the three-point test arrangement along with the corresponding employed instrumentation. The investigated beam specimens had a total length of 600 mm and overhung each end by 50 mm beyond the centrelines of the supports, resulting in a clear beam span of 500 mm. The span-to-height ratio was fixed and equal to 10 representing the proportions of actual beams and being sufficiently high to ensure a primary flexural response without any shear effect [31]. Steel rollers were used to form the simply-supported boundary conditions allowing free rotation about the in-plane bending axis, as well as free longitudinal displacement of the specimen's ends. For the bare specimens, wooden blocks with dimensions equal to the internal ones of the considered cross-sections were inserted within the tubes at the loading point and at both supports to prevent the occurrence of web crippling due to localised stress concentration. A Maves servo-controlled hydraulic testing machine with 600 kN capacity was used to perform the tests at 0.8 mm/min cross-head displacement rate. The loading was applied at the mid-span of the specimen until failure occurred.

To measure the extreme compressive and tensile strains during testing, two linear electrical resistance strain gauges were attached to the top and bottom flanges of each cross-section and at 20 mm distance from the mid-span. In addition, one linear variable displacement transducer (LVDT) was placed at the midspan to monitor the vertical deflection, and two inclinometers were located at the supports to measure the end rotations, as shown in Figs. 7 and 8. The applied load, strains, displacements and end rotations were recorded using a data acquisition system at 2 s intervals.

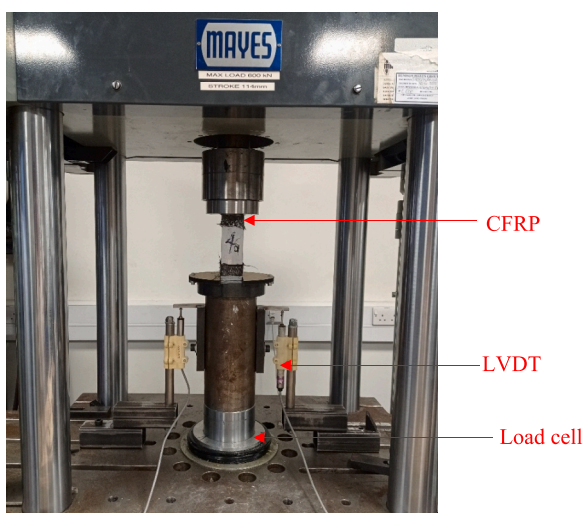


Fig. 6. Typical stub column test set-up.

## 3. Stub column test results and discussion

### 3.1. Failure modes

For the tested stub columns, the governing failure mode was local buckling. Typical failure modes are shown in Fig. 9. Fig. 9(a) displays the  $50.8 \times 50.8 \times 1.6$ -a specimen which failed due to elastic local buckling, occurring almost in the mid-height of the specimen. This was expected, since this was the slenderest cross-section (higher  $B/t$ ), and thus its cross-sectional capacity was limited by local buckling. Note that a slender cross-section fails due to local buckling before the attainment of its yield strength, whilst a stocky cross-section (lower  $B/t$ ) is capable of reaching its yield strength without presence of local instabilities. Fig. 9(b) and 9(c) present typical failure modes of GCFAT and CFAT specimens. After the execution of the GCFAT and CFAT tests, the aluminium tube was removed to inspect the crack patterns of the infill. Fig. 10 depicts the resulting crack patterns in  $50.8 \times 50.8 \times 4.8$ -GC-a and  $50.8 \times 50.8 \times 4.8$ -C-a specimens. It can be seen that the type of the infill has negligible influence on the failure mode. Infill crushing along with separation of the aluminium constituent plates was observed in the locations where buckling occurred. It is noteworthy that similar failure modes have also been observed for concrete-filled steel tubes [6,13,62,63].

### 3.2. Load-end shortening curves

The obtained load versus end shortening ( $F$ - $d$ ) curves of the tested specimens are plotted in Fig. 11, where the horizontal axis represents the end shortening  $d$  as average value measured from both LVDTs and the vertical axis represents the applied load  $F$ . In these graphs, black, green and red lines correspond to BAT, GCFAT and CFAT specimens, respectively. The key experimental results including the maximum recorded load ( $F_{u,Exp}$ ) and the corresponding end shortening ( $d_{u,Exp}$ ) are summarised in Table 6.

As can be seen, the initial behaviour of the BAT specimens is linear elastic. This is followed by a nonlinear elastic region up to yielding. Upon the attainment of the ultimate strength, the curves' slope decreases with increasing end shortening. The  $50.8 \times 50.8 \times 1.6$  specimen comprising the slenderest cross-section, exhibited its ultimate load level at the lowest  $d$  due to local buckling failure occurrence. In specimens with stockier cross-sections, the delay of local buckling allowed for deformation into the strain-hardening range and the achievement of ultimate loads higher than the yield load. In the case of the stockiest  $50.8 \times 50.8 \times 4.8$  specimen, the obtained ultimate load was even higher than the yield load, owing to the increased cross-sectional areas arising from the Poisson effect [64].

The cross-sectional response of both GCFAT and CFAT specimens was quite similar consisting of three stages. During the first stage (elastic), there is no interaction between the aluminium tube and the geopolymer concrete/OPC concrete infill and thus both components endure the applied load independently. Moreover, a small gap may appear between the aluminium tube and the geopolymer concrete/OPC concrete infill since the initial lateral expansion of the infill is smaller than that of the aluminium tube owing to the difference in Poisson's ratio of the two materials. In the following stage (elastic-plastic), as the loading increases, the lateral expansion of the infill gradually becomes greater than that of the aluminium tube until both components contact each other. That moment, interaction between the aluminium tube and the geopolymer concrete/OPC concrete develops and particularly the aluminium tube provides confining pressure to the infill. In the third stage (strain-hardening/softening), the GCFAT and CFAT stub columns continue to endure loading for increasing deformation owing to the confinement effect. Similarly to BAT specimens, it can be observed that composite specimens with stockier aluminium cross-sections, exhibited higher ductility, failing at larger displacement values. Comparing the obtained curves for  $50.8 \times 50.8 \times 4.8$ -GC (see Fig. 11(d)) and  $50.8 \times$

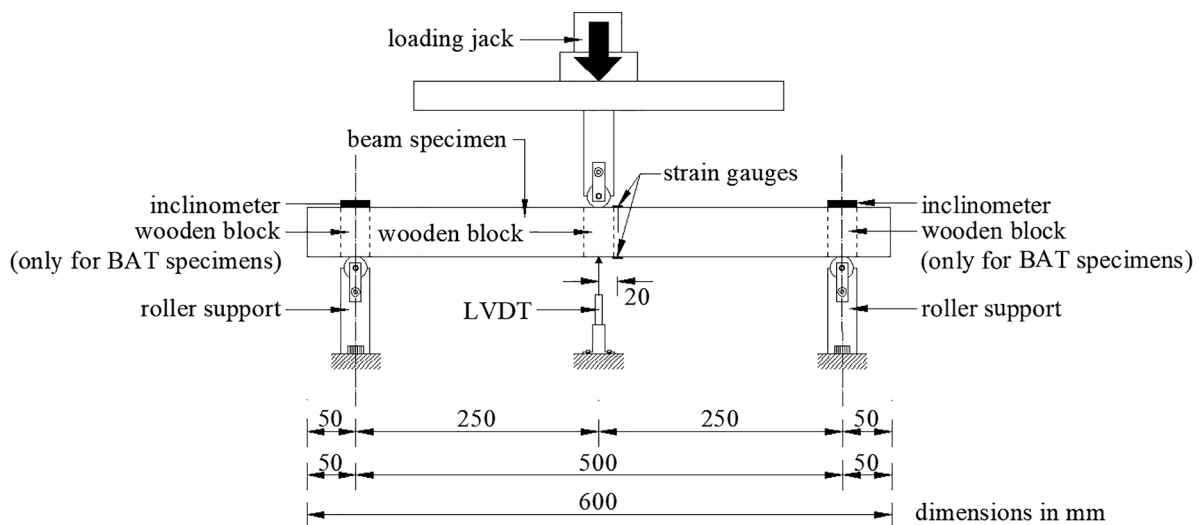


Fig. 7. Schematic illustration of the three-point bending test arrangement and instrumentation.



Fig. 8. Typical three-point bending test set-up.

50.8 × 1.6-GC specimens (see Fig. 11 (a)), it can be seen that the former one failed at 12.21 mm end shortening which is more than 6 times larger than that of the latter one. Moreover, specimens with thicker cross-sections exhibited higher elastic stiffness compared to their thinner counterparts.

Overall, it can be seen in Fig. 11 that the addition of the OPC concrete/geopolymer concrete infill increased the strength and ductility of all studied sections compared to the BAT specimens, particularly for sections comprising slender aluminium tubes. Additional discussion with respect to the effect of infill is included in the following section.

### 3.3. Effect of infill type

The effect of filling the aluminium tubes with geopolymer concrete/OPC concrete on their ultimate strength  $F_{u,Exp}$  and deformation at failure  $d_{u,Exp}$  is evaluated utilising the experimentally obtained results. Particularly, Table 7 presents the percentage increase  $[(F_{u,Exp,GCFAT} \text{ or } F_{u,Exp,CFAT}) - F_{u,Exp,BAT}] / F_{u,Exp,BAT}$  in ultimate strength for each GCFAT and

CFAT specimen with regards to the BAT specimens. In Fig. 12, the average percentage strength increase between the two replicate tests (a, b) are presented in chart form for each studied cross-section.

For both GCFAT and CFAT specimens, the highest strength increase was observed for the section 50.8 × 50.8 × 1.6, where the infill significantly delayed the occurrence of local buckling, resulting in quite higher ultimate strengths. Compared to the bare specimens, the addition of geopolymer concrete infill increased the strength by 91.0%, 95.7% for the two studied 50.8 × 50.8 × 1.6 sections, whilst for the same cross-section a similar strength increase (87.7%, 98.5%) was noted for the OPC concrete infill. For both infills, the lowest increase has been observed for the 50.8 × 50.8 × 4.8 cross-section. This can be related to the fact that this specimen comprises stocky aluminium plate elements, providing significant resistance to local buckling and thus the increased strength owing to the infill led to relatively small additional increase of the ultimate load. Moreover, for the two stockier specimens (50.8 × 50.8 × 3.3 and 50.8 × 50.8 × 4.8), the strength increase was observed to be higher for the OPC concrete compared to the geopolymer concrete one. In particular, for specimen 50.8 × 50.8 × 4.8 the strength increase had an average value of 16.5% and 23% for GCFAT and CFAT respectively. The same values were equal to 31.1% and 43.9% for GCFAT and CFAT respectively for specimen 50.8 × 50.8 × 3.3. This effect can be related to the higher compressive strength of the OPC concrete infill and its contribution to the overall strength, which indeed lessens for sections with higher  $B/t$ , where the main factor for increased strength is the resistance to local buckling offered due to the infill. In these slender sections, the GCFAT specimens presented slightly higher average strength increase (by 0.2% and 2.1% for 50.8 × 50.8 × 1.6 and 50.8 × 50.8 × 2.7, respectively) compared to the CFAT ones.

The percentage increase in displacement at failure  $[(d_{u,Exp,GCFAT} \text{ or } d_{u,Exp,CFAT}) - d_{u,Exp,BAT}] / d_{u,Exp,BAT}$  for each GCFAT and CFAT specimen is also presented in Table 7 and Fig. 12. Overall, it is shown that with the addition of the infill, the displacement at which failure is noted, increases. This is more pronounced for the slenderest cross-section, reaching values over 200% increase for specimen 50.8 × 50.8 × 1.6-C-a. For the most slender cross-section, CFAT specimens presented higher average increase (187.8%) in the displacement at failure compared to GCFAT counterparts (161.3%). However, it is noteworthy, that for the other three sections, the average value of the displacement at failure appeared to be generally higher for the GCFAT than the CFAT ones (see specimens 50.8 × 50.8 × 2.7, 50.8 × 50.8 × 3.3, 50.8 × 50.8 × 4.8 at Fig. 12 (b)).

Overall, the experimental results demonstrate that filling the aluminium tubes with geopolymer concrete has equally good response



(a) 50.8×50.8×1.6-a      (b) 50.8×50.8×4.8-GC-a      (c) 50.8×50.8×4.8-C-a

Fig. 9. Typical failure modes of stub columns: (a) BAT; (b) GCFAT; (c) CFAT.



(a) 50.8×50.8×4.8-C-a      (b) 50.8×50.8×4.8-GC-a

Fig. 10. Crack patterns of the infill for typical CFAT and GCFAT specimens.

compared to filling them with OPC concrete. This means that in composite aluminium-concrete sections, the concrete infill can be replaced by geopolymer concrete infill, which is a more sustainable material, without sacrificing the ultimate strength of the section.

#### 4. Beam test results and discussion

##### 4.1. Failure modes

Fig. 13 presents the obtained typical failure modes of BAT, GCFAT and CFAT and specimens. The predominant failure modes observed for the BAT specimens were material yielding and local buckling on the upper compressive flange. Specimen 50.8 × 50.8 × 1.6 (Fig. 13(a)) failed due to elastic local buckling on the upper flange, which occurred at the vicinity of the loading point at the midspan where the stress concentration was higher due to the presence of the moment gradient. The remaining BAT specimens failed due to material yielding accompanied by inelastic local buckling on the upper flange.

In GCFAT and CFAT beams, the presence of the infill helped the aluminium tubes to resist the developed local deformations allowing for full development of aluminium alloy’s plasticity. Most specimens exhibited significant inelastic in-plane deformations and failed by tensile fracture at the lower flange of the aluminium tube at the midspan

due to exceedance of the aluminium alloy’s tensile fracture strain (see Fig. 13(c)). Moreover, in specimens with slenderer aluminium sections, pronounced inelastic local buckling on the upper flange of the aluminium tube was observed prior to failure by tensile fracture.

After the execution of the tests of the CFAT and GCFAT beams, the aluminium tube around the midspan was removed to inspect the crack patterns of the infill. Fig. 14 shows the resulting crack patterns in 50.8 × 50.8 × 4.8-GC and 50.8 × 50.8 × 4.8-C specimens. In both specimens, the flexural cracks are uniformly distributed around the midspan and along the concrete tensile fibre of the specimens.

##### 4.2. Bending moment-midspan deflection/end-rotation curves

The obtained bending moment versus midspan deflection ( $M-\delta$ ) curves of the tested specimens are plotted in Fig. 15 (green-GCFAT, red-CFAT, black-BAT). In these graphs, the horizontal axis represents the vertical deflection  $\delta$  at the midspan measured from the LVDT and the vertical axis represents the bending moment  $M$  at the midspan of the specimen calculated by formula  $M = PL_e/4$  where  $P$  is the applied load and  $L_e$  is the length of the clear span ( $L_e = 500$  mm in this study).

As can be seen, initially the BAT specimens exhibit a linear elastic behaviour followed by a nonlinear region up to the plastic moment resistance. Upon the attainment of the ultimate bending moment  $M_u$ , the curves’ slope decreases with increasing vertical deflections. It is noteworthy that the descending branch of the 50.8 × 50.8 × 1.6 specimen is comparatively steeper owing to the local buckling occurrence which led to significant loss of strength. The obtained flexural response of both CFAT and GCFAT specimens was quite similar consisting of three stages. During the first stage (elastic), the aluminium tube and the geopolymer concrete/OPC concrete infill bear load independently. Yielding of the aluminium tube also occurs at this stage. In the following stage (elastic–plastic), as the bending moment increases, the infill cracks and its volume gradually becomes greater. After some time, the two components come in contact and the aluminium tube provides confining pressure to the infill. Expansion of infill cracking at the tensile side results in degradation of the flexural stiffness. However, interaction between the aluminium tube and the infill effectively hinders the development of infill cracking along the cross-sectional depth offering effective support and thus leading to high deformation capacity of the GCFAT/CFAT beams. In the third stage (plastic), the GCFAT/CFAT beams continue to sustain bending moment for increasing deformation owing to the confinement provided by the aluminium tube to the cracked infill. Finally, failure occurs when the developed strains at the tensile (lower) flange of the aluminium tube at the midspan exceed the aluminium alloy’s tensile fracture strain  $\epsilon_f$ . Similar observations can be

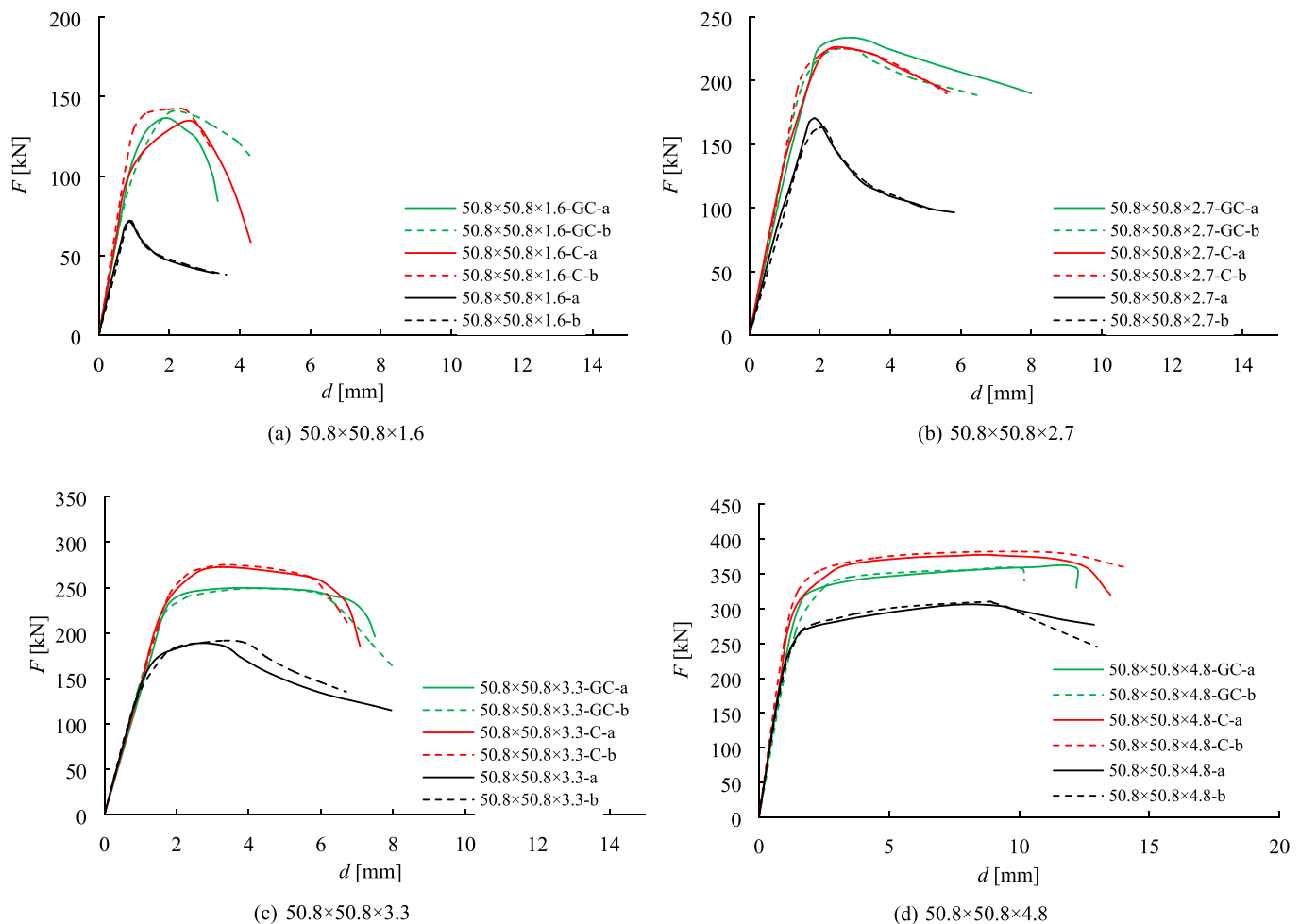


Fig. 11. Load-end shortening curves of stub column tests.

made from Fig. 16, where the bending moment is plotted versus the end rotation, as obtained by the inclinometers. The key experimental results including the ultimate bending moment  $M_{u,Exp}$  and the corresponding midspan deflection  $\delta_{u,Exp}$  and end-rotation  $\theta_{u,Exp}$  are summarised in Table 8. It is noted that for GCFAT and CFAT specimens, the reported  $M_u$  values are the maximum recorded values.

#### 4.3. Effect of infill type

The experimentally obtained ultimate loads are utilised to evaluate the effect of filling the aluminium tubes with geopolymer concrete/OPC concrete on their ultimate flexural strength and the corresponding displacement and rotation at failure. As shown in Fig. 16, the presence of the geopolymer concrete/OPC concrete infill improved the strength and deformation capacity of the members compared to the BAT ones and prevented a potential failure due to local buckling occurrence.

To further visualise the effect of infill, Table 9 presents the percentage increase  $[(M_{u,Exp,GCFAT} \text{ or } M_{u,Exp,CFAT}) - M_{u,Exp,BAT}] / M_{u,Exp,BAT}$  in flexural strength, the percentage increase  $[(\delta_{u,Exp,GCFAT} \text{ or } \delta_{u,Exp,CFAT}) - \delta_{u,Exp,BAT}] / \delta_{u,Exp,BAT}$  in displacement at failure and the percentage increase  $[(\theta_{u,Exp,GCFAT} \text{ or } \theta_{u,Exp,CFAT}) - \theta_{u,Exp,BAT}] / \theta_{u,Exp,BAT}$  in rotation at failure for each GCFAT and CFAT specimen compared to the counterpart BAT specimens. In Fig. 17, the results are visualised with respect to the corresponding nominal  $B/t$  values.

As shown in Fig. 17(a), the presence of the infill improved the flexural performance of the BAT specimens. Particularly, both the geopolymer concrete and concrete infill increased approximately 50% the flexural strength of  $50.8 \times 50.8 \times 1.6$  section compared to the bare

counterpart. The lowest flexural strength increase was observed for the  $50.8 \times 50.8 \times 4.8$  section (14.1% for GCFAT and 10.2% for CFAT). GCFAT recorded a generally higher strength increase compared to the CFAT ones in most cases.

Fig. 17 (b) and 17 (c) show that both types of infill significantly improved the BAT specimens' displacement and rotation capacity. The percentage increase of the displacement at failure was in the range of 66.8%–173.7% and 67.2%–226.8% for GCFAT and CFAT specimens respectively. The percentage increase of the rotation at failure was in the range of 73.4%–189.3% and 84.1%–227.2% for GCFAT and CFAT specimens respectively. The improvement was generally less pronounced in GCFAT specimens that can be related to the geopolymer concrete's higher brittleness [32]. For example, in case of the slenderest section, i.e.,  $50.8 \times 50.8 \times 1.6$ , the geopolymer concrete infill increased the displacement and rotation at failure by 173.7% and 189.3%, respectively. For the same cross-section, the concrete infill resulted in 226.8% and 227.2% increase, respectively. In a similar manner with the strength increase, the displacement and rotation capacity increase was more pronounced for sections with higher  $B/t$ .

Overall, filling the aluminium tubes with geopolymer concrete has satisfactory and equally good response compared to filling them with OPC concrete.

#### 5. Design recommendations

In this section the experimental results are utilised to make design recommendations for the strength prediction of GCFAT and CFAT stub columns and beams. In absence of codified design rules for the

**Table 6**  
Results obtained from stub column tests.

Specimen	$F_{u,Exp}$ (kN)	$d_{u,Exp}$ (mm)
<i>BAT stub columns</i>		
50.8 × 50.8 × 1.6-a	71.12	0.90
50.8 × 50.8 × 1.6-b	71.98	0.88
50.8 × 50.8 × 2.7-a	170.47	1.84
50.8 × 50.8 × 2.7-b	163.18	2.04
50.8 × 50.8 × 3.3-a	188.83	2.67
50.8 × 50.8 × 3.3-b	191.55	3.12
50.8 × 50.8 × 4.8-a	305.81	7.69
50.8 × 50.8 × 4.8-b	310.15	8.90
<i>GCFAT stub columns</i>		
50.8 × 50.8 × 1.6-GC-a	136.63	1.93
50.8 × 50.8 × 1.6-GC-b	140.00	2.71
50.8 × 50.8 × 2.7-GC-a	233.86	2.90
50.8 × 50.8 × 2.7-GC-b	224.97	2.90
50.8 × 50.8 × 3.3-GC-a	249.53	3.96
50.8 × 50.8 × 3.3-GC-b	249.11	4.24
50.8 × 50.8 × 4.8-GC-a	359.65	12.21
50.8 × 50.8 × 4.8-GC-b	358.00	10.09
<i>CFAT stub columns</i>		
50.8 × 50.8 × 1.6-C-a	134.33	2.68
50.8 × 50.8 × 1.6-C-b	142.00	2.43
50.8 × 50.8 × 2.7-C-a	226.54	2.50
50.8 × 50.8 × 2.7-C-b	225.16	2.34
50.8 × 50.8 × 3.3-C-a	272.48	3.22
50.8 × 50.8 × 3.3-C-b	275.00	3.50
50.8 × 50.8 × 4.8-C-a	375.43	9.08
50.8 × 50.8 × 4.8-C-b	382.00	10.10

**Table 7**  
Effect of the geopolymer concrete/OPC concrete infill compared with the BAT stub columns.

Specimen	$[(F_{u,Exp,GCFAT} \text{ or } F_{u,Exp,CFAT}) / F_{u,Exp,BAT}] / F_{u,Exp,BAT}$	$[(d_{u,Exp,GCFAT} \text{ or } d_{u,Exp,CFAT}) / d_{u,Exp,BAT}] / d_{u,Exp,BAT}$
<i>GCFAT stub columns</i>		
50.8 × 50.8 × 1.6-GC-a	91.0%	117.6%
50.8 × 50.8 × 1.6-GC-b	95.7%	205.1%
50.8 × 50.8 × 2.7-GC-a	40.2%	49.3%
50.8 × 50.8 × 2.7-GC-b	34.9%	49.5%
50.8 × 50.8 × 3.3-GC-a	31.2%	37.0%
50.8 × 50.8 × 3.3-GC-b	31.0%	46.7%
50.8 × 50.8 × 4.8-GC-a	16.8%	47.3%
50.8 × 50.8 × 4.8-GC-b	16.2%	21.7%
<i>CFAT stub columns</i>		
50.8 × 50.8 × 1.6-C-a	87.7%	201.9%
50.8 × 50.8 × 1.6-C-b	98.5%	173.6%
50.8 × 50.8 × 2.7-C-a	35.8%	28.9%
50.8 × 50.8 × 2.7-C-b	35.0%	20.6%
50.8 × 50.8 × 3.3-C-a	43.3%	11.4%
50.8 × 50.8 × 3.3-C-b	44.6%	21.0%
50.8 × 50.8 × 4.8-C-a	21.9%	9.5%
50.8 × 50.8 × 4.8-C-b	24.0%	21.8%

prediction of the cross-sectional capacities of composite aluminium-concrete and aluminium-geopolymer concrete cross-sections, the present study will provide design recommendations on the basis of the design formulae for composite steel–concrete cross-sections available in EN 1994-1-1 (EC4) [49]. Particularly, this study proposes the replacement of the material properties of steel by those of the examined aluminium alloy; for the GCFAT cross-sections the replacement of the material properties of concrete by those of the geopolymer concrete is proposed. Note that all partial safety factors are set equal to unity for these assessments.

5.1. Stub columns

The following equation of EC4 [49] is used to calculate the cross-sectional capacity ( $F_{u,prop}$ ) of square and rectangular GCFAT and CFAT sections:

$$F_{u,prop} = A_a \sigma_{0.2} + 0.85 A_c f_{ck} \tag{1}$$

where  $A_c$  and  $f_{ck}$  are the cross-sectional area and the characteristic compressive cylinder strength of the geopolymer concrete/OPC concrete infill.  $A_a$  is the cross-sectional area of the aluminium tube for non-slender cross-sections [48].

It is noted that for aluminium structures, EC9 [48] adopts the cross-section classification for the treatment of local buckling in aluminium cross-sections under compression. Particularly, it defines slenderness limits for the constituent plate elements enabling to identify the extent to which the cross-sectional capacity is limited by the local buckling resistance. The limits are defined based on the material Class A or B (the herein examined 6082-T6 aluminium alloy is Class A) and on the cross-sectional slenderness ratio. Class 1 or ductile cross-sections are those which can develop their plastic resistance without the presence of local instabilities. Class 2 or compact cross-sections are those which can develop their plastic resistance with the presence of local instabilities in the plastic range. Class 3 or semi-compact cross-sections are those which can develop their elastic resistance, whilst local buckling prevents them from getting into the plastic range. Class 4 or slender cross-sections are those which cannot reach yielding because of premature local buckling in the elastic range. As also observed in Sections 3-4, Class 4 sections presented a more significant strength increase compared to Class 1–3 sections, due to the delay of local buckling. Given the limited data on slender sections whose local buckling performance changes due to the material infill, the design recommendations hereafter is only based on specimens with non-slender aluminium tubes.

Implementing the formula of Equation (1), the ultimate proposed over experimental strength ratio ( $F_{u,prop}/F_{u,Exp}$ ) for each GCFAT and CFAT tested cross-section are listed in Table 10. The obtained mean value of the  $F_{u,prop}/F_{u,Exp}$  ratio is equal to 0.89, whilst all values of the strength ratios are lower than unity, suggesting safe design strength predictions. Moreover, the resulting coefficients of variation (COV) equal to 0.06 indicates relatively low scatter and satisfactory design consistency. It can be concluded that the combined formulae proposed herein for the strength prediction of GCFAT and CFAT cross-sections under uniform compression provide reasonably accurate results with good consistency.

5.2. Beams

The flexural capacity of square and rectangular GCFAT and CFAT members ( $M_{u,prop}$ ) can be obtained using the Equation (2) of EC4 [49]:

$$M_{u,prop} = (W_{pla} - W_{pla,n}) \sigma_{0.2} + 0.5 (W_{plc} - W_{plc,n}) f_{ck} \tag{2}$$

where  $W_{pla}$  and  $W_{plc}$  are the plastic section moduli of the aluminium tube and geopolymer concrete/concrete, respectively, given by the Eqs. (3) and (4), respectively.  $W_{pla,n}$  and  $W_{plc,n}$  are the plastic section moduli of the aluminium tube and geopolymer concrete/concrete from  $2h_n$ ,

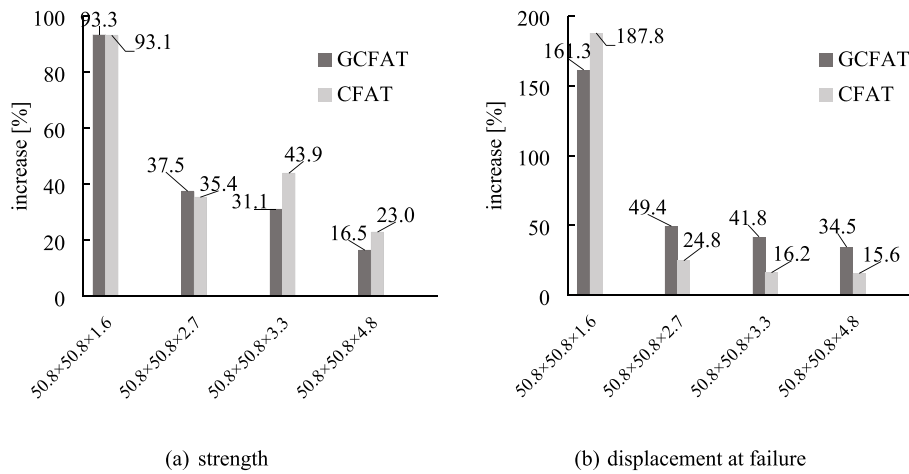


Fig. 12. Effect of the concrete infill compared to BAT stub columns, based on average values between the two replicates: (a) strength increase; (b) displacement at failure.

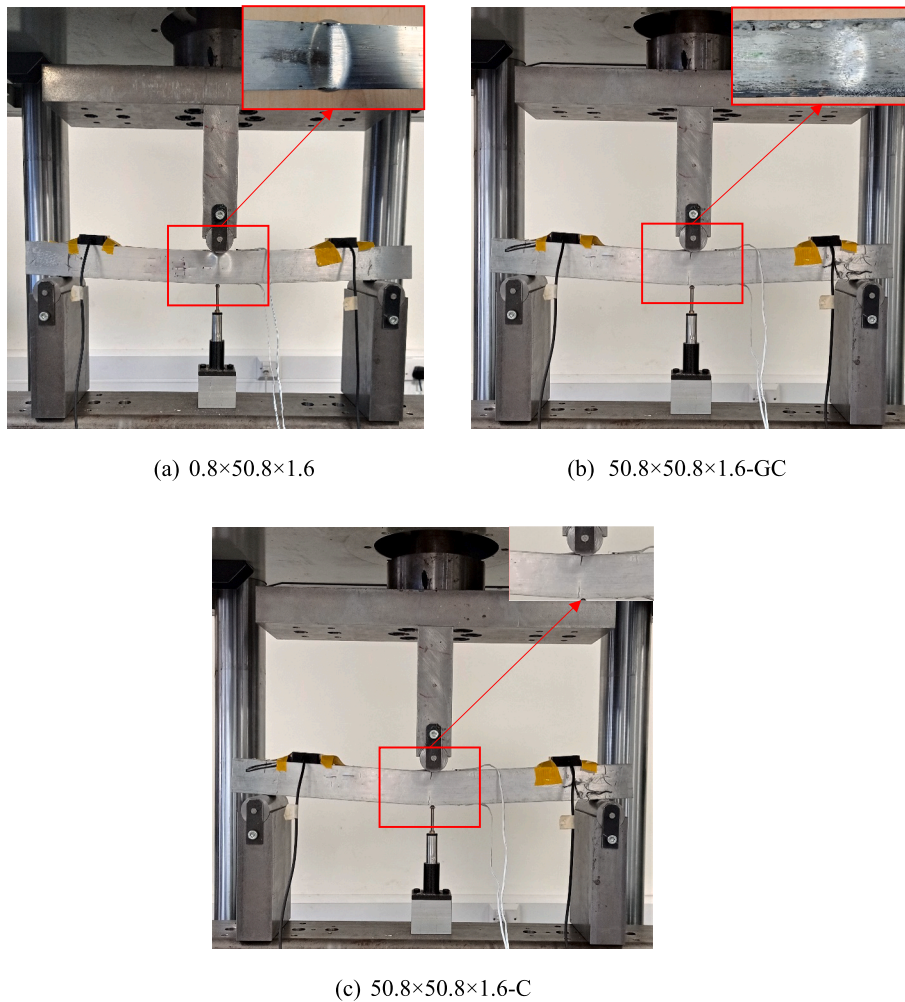
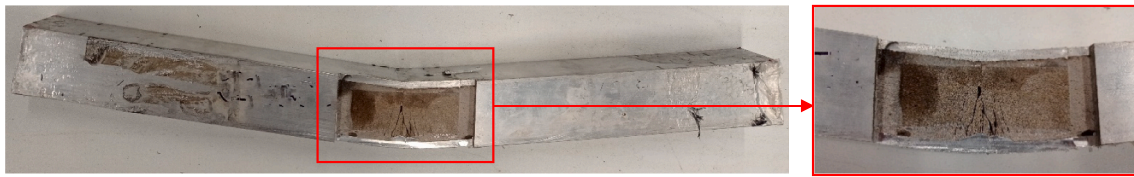


Fig. 13. Typical failure modes of beams: (a) BAT; (b) GCFAT; (c) CFAT.

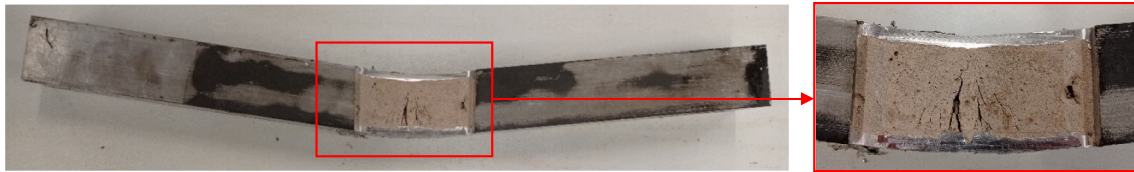
respectively, given by the Eqs. (5) and (6), respectively. The term  $h_n$  is the location of the neutral axis calculated by the Equation (7), where  $A_c$  and  $f_{ck}$  are the area and the compressive cylinder strength of the geopolymer concrete/concrete, respectively. In Eqs. (3) and (4),  $r_{int}$  is the internal corner radius of the aluminium tube which is zero herein.

$$W_{pla} = \frac{BD^2}{4} - \frac{2}{3}(r_{int} + t)^3 - (r_{int} + t)^2(4 - \pi)\left(\frac{D}{2} - t - r_{int}\right) - W_{plc} \quad (3)$$

$$W_{plc} = \frac{(B - 2t)(D - 2t)^2}{4} - \frac{2}{3}r_{int}^3 - r_{int}^2(4 - \pi)\left(\frac{D}{2} - t - r_{int}\right) \quad (4)$$

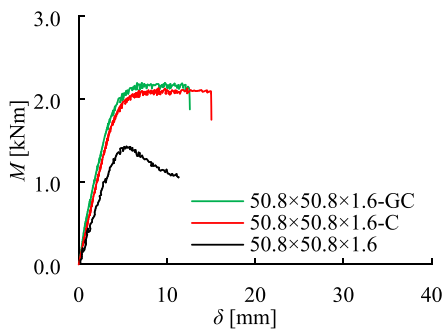


(a) 50.8×50.8×4.8-GC

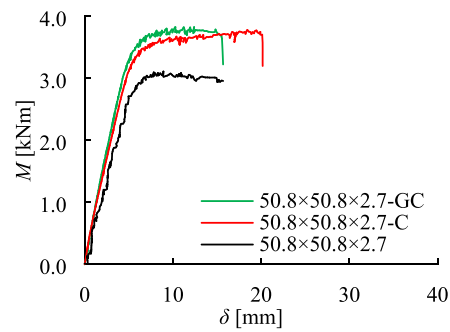


(b) 50.8×50.8×4.8-C

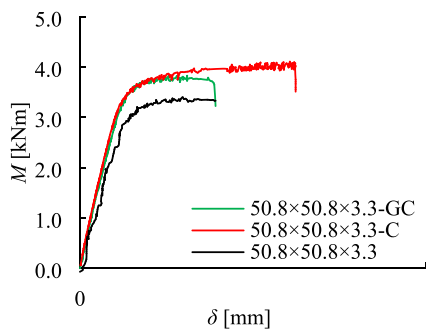
Fig. 14. Crack patterns of typical CFAT and GCFAT specimens.



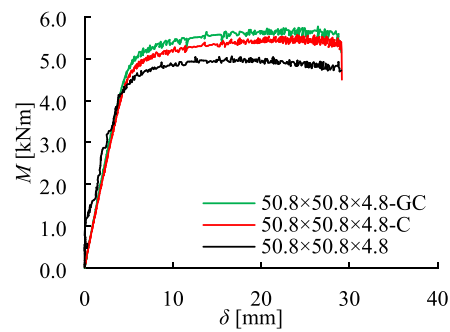
(a) 50.8×50.8×1.6



(b) 50.8×50.8×2.7



(c) 50.8×50.8×3.3



(e) 50.8×50.8×4.8

Fig. 15. Experimental bending moment versus midspan deflection curves.

$$W_{pl,a,n} = Bh_n^2 - W_{pl,c,n} \tag{5}$$

$$W_{pl,c,n} = (B - 2t)h_n^2 \tag{6}$$

$$h_n = \frac{A_c f_{ck}}{2Bf_{ck} + 4t(2\sigma_{0.2} - f_{ck})} \tag{7}$$

Table 11 presents the proposed over experimental ultimate bending moment ratio ( $M_{ub,prop}/M_{u,Exp}$ ) for each GCFAT and CFAT tested cross-section. As can be seen, the proposed ultimate bending moments  $M_{ub,prop}$  for both GCFAT and CFAT beam specimens appear to be safe as

the corresponding mean values of the  $M_{ub,prop}/M_{u,Exp}$  ratio are lower than unity. Moreover, the resulting low coefficients of variation (COV) denote low scatter and thereby adequate design consistency. Overall, the combined formulae proposed herein for the design of flexural GCFAT and CFAT members provide good predictions with reasonable consistency.

## 6. Conclusions

The current study proposed a new composite structural cross-section with low carbon footprint and investigated experimentally its potential

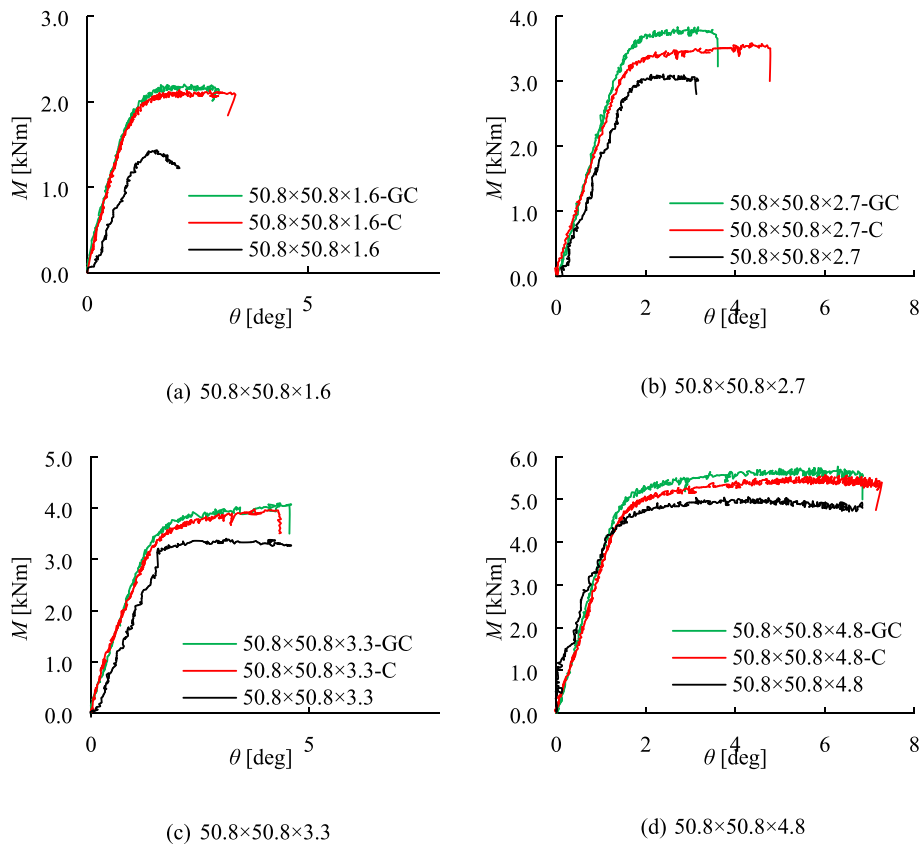


Fig. 16. Experimental bending moment versus end-rotation curves.

Table 8

Key results obtained from three-point bending tests.

Specimen	$M_{u,Exp}$ [kNm]	$\delta_{u,Exp}$ [mm]	$\theta_{u,Exp}$ [deg]
<b>BAT beams</b>			
50.8 × 50.8 × 1.6	1.43	4.60	1.03
50.8 × 50.8 × 2.7	3.11	8.72	2.14
50.8 × 50.8 × 3.3	3.40	10.85	2.40
50.8 × 50.8 × 4.8	5.05	17.44	3.95
<b>GCFAT beams</b>			
50.8 × 50.8 × 1.6-GC	2.20	12.60	2.98
50.8 × 50.8 × 2.7-GC	3.83	15.69	3.80
50.8 × 50.8 × 3.3-GC	4.11	18.00	4.36
50.8 × 50.8 × 4.8-GC	5.76	29.08	6.85
<b>CFAT beams</b>			
50.8 × 50.8 × 1.6-C	2.13	15.04	3.37
50.8 × 50.8 × 2.7-C	3.78	20.17	4.97
50.8 × 50.8 × 3.3-C	4.11	24.96	4.59
50.8 × 50.8 × 4.8-C	5.57	29.15	7.27

to enhance the structural performance of BAT cross-sections. For this purpose, a total of 24 stub columns (8 BAT, 8 GCFAT and 8 CFAT) were subjected to uniform compression and 12 specimens (4 BAT, 4 GCFAT and 4 CFAT) were subjected to three-point bending. Based on the experimental results, the following conclusions are drawn:

- (1) In stub columns, the governing failure mode was local buckling. In beams, the BAT specimens failed due to material yielding accompanied by inelastic local buckling on the upper flange, whilst the specimen with the slenderest cross-section failed due to elastic local buckling on the upper flange. GCFAT and CFAT

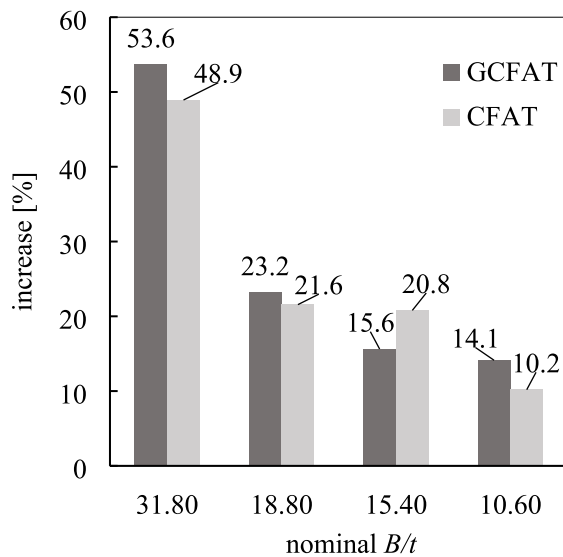
Table 9

Effect of the geopolymer concrete/OPC concrete infill compared with the BAT beams.

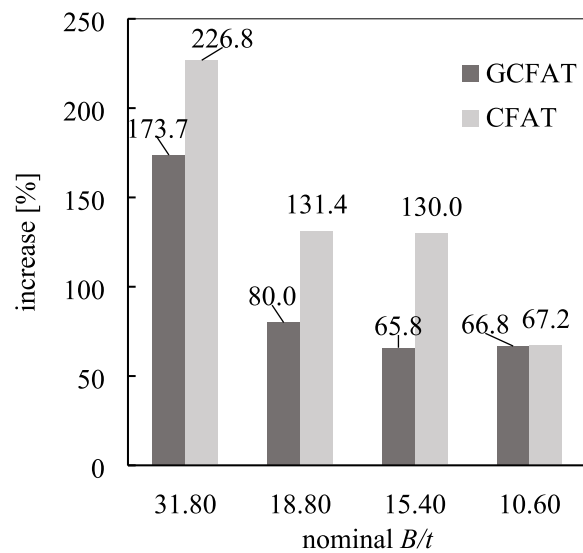
Specimen	$[(M_{u,Exp,GCFAT} \text{ or } M_{u,Exp,CFAT}) - M_{u,Exp,BAT}] / M_{u,Exp,BAT}$	$[(\delta_{u,Exp,GCFAT} \text{ or } \delta_{u,Exp,CFAT}) - \delta_{u,Exp,BAT}] / \delta_{u,Exp,BAT}$	$[(\theta_{u,Exp,GCFAT} \text{ or } \theta_{u,Exp,CFAT}) - \theta_{u,Exp,BAT}] / \theta_{u,Exp,BAT}$
<b>GCFAT beams</b>			
50.8 × 50.8 × 1.6-GC	53.6%	173.7%	189.3%
50.8 × 50.8 × 2.7-GC	23.2%	80.0%	77.6%
50.8 × 50.8 × 3.3-GC	15.6%	65.8%	81.7%
50.8 × 50.8 × 4.8-GC	14.1%	66.8%	73.4%
<b>CFAT beams</b>			
50.8 × 50.8 × 1.6-C	48.9%	226.8%	227.2%
50.8 × 50.8 × 2.7-C	21.6%	131.4%	132.2%
50.8 × 50.8 × 3.3-C	20.8%	130.0%	91.3%
50.8 × 50.8 × 4.8-C	10.2%	67.2%	84.1%

beams exhibited significant inelastic in-plane deformations and failed by tensile fracture at the lower flange of the aluminium tube.

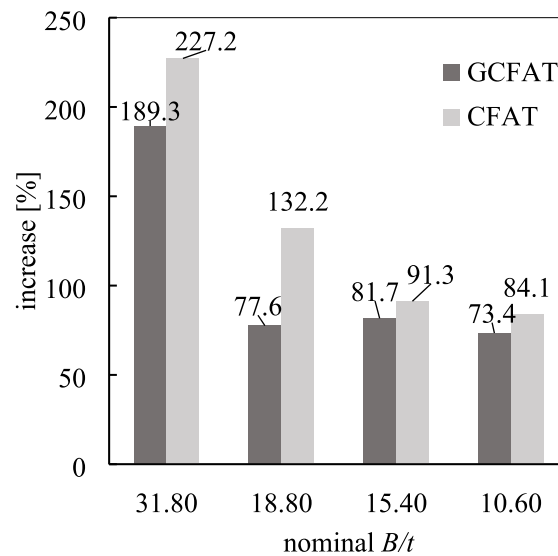
- (2) Both types of infill, i.e., GC or OPC concrete, enhanced notably the performance of the aluminium members, as the presence of the infill braced the aluminium tubes to resist the developed deformations, thus allowing for higher strength and displacement compared to BAT specimens.



(a) strength



(b) displacement at failure



(c) rotation at failure

Fig. 17. Effect of the concrete infill compared to BAT beams: (a) strength increase; (b) displacement at failure; (c) rotation at failure.

Table 10  
Proposed design strengths for GCFAT and CFAT cross-sections.

Specimen	$F_{u,prop}/F_{u,Exp}$
50.8 × 50.8 × 2.7-GC-a	0.87
50.8 × 50.8 × 2.7-GC-b	0.92
50.8 × 50.8 × 3.3-GC-a	0.88
50.8 × 50.8 × 3.3-GC-b	0.89
50.8 × 50.8 × 4.8-GC-a	0.84
50.8 × 50.8 × 4.8-GC-b	0.84
50.8 × 50.8 × 2.7-C-a	0.99
50.8 × 50.8 × 2.7-C-b	0.98
50.8 × 50.8 × 3.3-C-a	0.88
50.8 × 50.8 × 3.3-C-b	0.87
50.8 × 50.8 × 4.8-C-a	0.84
50.8 × 50.8 × 4.8-C-b	0.83
mean	0.89
COV	0.06

Table 11  
Proposed design strengths for GCFAT and CFAT beams.

Specimen	$M_{u,prop}/M_{u,Exp}$
50.8 × 50.8 × 2.7-GC	0.83
50.8 × 50.8 × 3.3-GC	0.83
50.8 × 50.8 × 4.8-GC	0.81
50.8 × 50.8 × 2.7-C	0.87
50.8 × 50.8 × 3.3-C	0.85
50.8 × 50.8 × 4.8-C	0.86
mean	0.84
COV	0.03

(3) Compared to BAT specimens, the average strength increase was in the range of 16.5%–93.3% and 23%–93.1% for GCFAT and CFAT stub columns, respectively. In beams, the flexural strength

increase was in the range of 14.1%–53.6% for GCFAT beams and of 10.2%–48.9% for CFAT beams.

- (4) In both cases, the percentage strength increase was more pronounced for the slenderest aluminium cross-sections. This is attributed to the delay to local buckling offered by the infill in sections with more slender aluminium tubes.
- (5) In absence of codified criteria for composite aluminium-geopolymer concrete cross-sections, the present study proposed adopting the design formulae of EC4 replacing the material properties of steel by those of aluminium alloy and of concrete by those of the geopolymer concrete. The proposed design methodology was found to be suitable for the composite cross-sections comprising non-slender aluminium sections, providing reasonably accurate strength predictions for both stub columns and beams.
- (6) Overall the present study demonstrated that the combination of structural aluminium alloys with geopolymer concrete can lead to a novel structurally efficient cross-section.
- (7) Future research is recommended in order to assess the corrosion resistance and durability performance of GC-aluminium members and compare it to that of OPC-aluminium members and to quantify the sustainability performance of the proposed composite member. Finally, the present study and the relevant conclusions are based on cross-sections of 50 mm width and the geopolymer concrete of approx. 30 MPa cube strength; further investigations on larger scale applications, different types of composite cross-sections and considering higher strength geopolymer concrete are recommended.

#### Declaration of Competing Interest

The authors declare that they have no known competing financial interests or personal relationships that could have appeared to influence the work reported in this paper.

#### Acknowledgements

The authors are grateful to the technicians of School of Civil Engineering and Built Environment and School of Engineering at Liverpool John Moores University for their valuable assistance.

#### References

- [1] Han LH, Li W, Bjorhovde R. Developments and advanced applications of concrete-filled steel tubular (CFST) structures: Members. *J Constr Steel Res* 2014;100:211–28.
- [2] Liu H, Wang Y, He M, Shi Y, Waisman H. Strength and ductility performance of concrete-filled steel tubular columns after long-term service loading. *Eng Struct* 2015;100:308–25.
- [3] Dong JF, Wang QY, Guan ZW. Structural behaviour of recycled aggregate concrete filled steel tube columns strengthened by CFRP. *Eng Struct* 2013;48:532–42.
- [4] Huang C, Han XL, Ji J, Tang JM. Behavior of concrete-filled steel tubular planar intersecting connections under axial compression, Part 1: Experimental study. *Eng Struct* 2010;32(1):60–8.
- [5] Zeghiche J, Chaoui K. An experimental behaviour of concrete-filled steel tubular columns. *J Constr Steel Res* 2005;61(1):53–66.
- [6] Guo L, Zhang S, Kim WJ, Ranzi G. Behavior of square hollow steel tubes and steel tubes filled with concrete. *Thin-Walled Struct* 2007;45(12):961–73.
- [7] Giakoumelis G, Lam D. Axial capacity of circular concrete-filled tube columns. *J Constr Steel Res* 2004;60(7):1049–68.
- [8] Wang Q, Zhao D, Guan P. Experimental study on the strength and ductility of steel tubular columns filled with steel-reinforced concrete. *Eng Struct* 2004;26(7):907–15.
- [9] Yu ZW, Ding FX, Cai CS. Experimental behavior of circular concrete-filled steel tube stub columns. *J Constr Steel Res* 2007;63(2):165–74.
- [10] Kwan AKH, Dong CX, Ho JCM. Axial and lateral stress-strain model for circular concrete-filled steel tubes with external steel confinement. *Eng Struct* 2016;117:528–41.
- [11] Lai MH, Ho JCM. A theoretical axial stress-strain model for circular concrete-filled-steel-tube columns. *Eng Struct* 2016;125:124–43.
- [12] Georgantzia E, Gkantou M, Kamaris GS. Aluminium alloys as structural material: A review of research. *Eng Struct* 2021;227:111372.
- [13] Zhou F, Young B. Tests of concrete-filled aluminum stub columns. *Thin-Walled Struct* 2008;46(6):573–83.
- [14] Australian/New Zealand Standard (AS/NZS) Aluminium structures part 1: Limit state design. AS/NZS 1664.1:1997. Standards Australia, Sydney, Australia; 1997.
- [15] The Aluminum Association (AA), Aluminum design manual. Washington, DC; 2020.
- [16] Zhou F, Young B. Concrete-filled aluminum circular hollow section column tests. *Thin-Walled Struct* 2009;47(11):1272–80.
- [17] Zhou F, Young B. Numerical analysis and design of concrete-filled aluminum circular hollow section columns. *Thin-Walled Struct* 2012;50(1):45–55.
- [18] Zhou F, Young B. Concrete-filled double-skin aluminum circular hollow section stub columns. *Thin-Walled Struct* 2018;133(September):141–52.
- [19] Wang FC, Zhao HY, Han LH. Analytical behavior of concrete-filled aluminum tubular stub columns under axial compression. *Thin-Walled Struct* 2019;140:21–30.
- [20] GB 50936-2014. Technical code for concrete filled steel tubular structures. 2014.
- [21] Ali SB, Kamaris GS, Gkantou M, Kansara KD. Concrete-filled and bare 6082-T6 aluminium alloy tubes under in-plane bending: Experiments, finite element analysis and design recommendations. *Thin-Walled Struct* 2022;172:108907.
- [22] Georgantzia E, Ali SB, Gkantou M, Kamaris GS, Kansara KD, Atherton W. Flexural buckling performance of concrete-filled aluminium alloy tubular columns. *Eng Struct* 2021;242:112546.
- [23] Ali SB, Kamaris GS, Gkantou M. Flexural behaviour of concrete-filled double skin aluminium alloy tubes. *Eng Struct* 2022;272:114972.
- [24] Feng R, Chen Y, Gong W. Flexural behaviour of concrete-filled aluminium alloy thin-walled SHS and RHS tubes. *Eng Struct* 2017;137:33–49.
- [25] Chen Y, Feng R, Xu J. Flexural behaviour of CFRP strengthened concrete-filled aluminium alloy CHS tubes. *Constr Build Mater* 2017;142:295–319.
- [26] Habert G, Espinose JB, Lacaille D, Roussel N. An environmental evaluation of geopolymer based concrete production: reviewing current research trends. *J Clean Prod* 2011;19(11):1229–38.
- [27] Hassan A, Arif M, Shariq M. Use of geopolymer concrete for a cleaner and sustainable environment e A review of mechanical properties and microstructure. *J Clean Prod* 2019;223:704–28.
- [28] Duxson P, Provis JL, Lukey GC, Van Deventer JSJ. The role of inorganic polymer technology in the development of 'green concrete'. *Cem Concr Res* 2007;37:1590–7.
- [29] Luukkonen T, Abdollahnejad Z, Ohenoja K, Kinnunen P, Illikainen M. Suitability of commercial superplasticizers for one-part alkali-activated blast-furnace slag mortar. *J Sustain Cem-Based Mater* 2019;8(4):244–57.
- [30] Adesanya E, Perumal P, Luukkonen T, Yliniemi J, Ohenoja K, Kinnunen P, et al. Opportunities to improve sustainability of alkali-activated materials: A review of side-stream based activators. *J Clean Prod* 2021;286:125558.
- [31] Mellado A, Catalán C, Bouzón N, Borrachero MV, Monz JM, Payá J. Carbon footprint of geopolymeric mortar: study of the contribution of the alkaline activating solution and assessment of an alternative route. *RSC Adv* 2014;4(45):23846–52.
- [32] Almalkawi AT, Hamadna S, Soroushian P. One-part alkali activated cement based volcanic pumice. *Constr Build Mater* 2017;152:367–74.
- [33] Kadhim A, Sadique M, Al-Mufti R, Hashim K. Developing One-Part Alkali-Activated metakaolin/natural pozzolan Binders using Lime Waste as activation Agent. *Adv Cem Res* 2021;33(8):342–56.
- [34] Kadhim A, Sadique M, Al-Mufti R, Hashim K. Long-term performance of novel high-calcium one-part alkali-activated cement developed from thermally activated lime kiln dust. *J Build Eng* 2020 Nov;1(32):101766.
- [35] Singh B, Ishwarya G, Gupta M, Bhattacharyya SK. Geopolymer concrete: A review of some recent developments. *Constr Build Mater* 2015;5:78–90.
- [36] Hassan A, Arif M, Shariq M. Use of geopolymer concrete for a cleaner and sustainable environment—A review of mechanical properties and microstructure. *J Clean Prod* 2019;223:704–28.
- [37] Khalid HR, Ha SK, Park SM, Kim GM, Lee HK. Interfacial bond behavior of FRP fabrics bonded to fiber-reinforced geopolymer mortar. *Compos Struct* 2015;134:353–68.
- [38] Lokuge WP, Sanjayan JG, Setunge S. Stress-strain model for laterally confined concrete. *J Mater Civ* 2005;176:607–16.
- [39] Lokuge W, Abousnina R, Herath N. Behaviour of geopolymer concrete-filled pultruded GFRP short columns. *J Compos Mater* 2019;53(18):2555–67.
- [40] Tennakoon C, Shayan A, Sanjayan JG, Xu A. Chloride ingress and steel corrosion in geopolymer concrete based on long term tests. *Mater Des* 2017;116:287–99.
- [41] Zainal FF, Ismail NHH, Hashim MFA, Daud YM, Abdullah MMAB. Corrosion Control by Using Aluminium as Sacrificial Anode Cathodic Protection (SACP) in Geopolymer Reinforced Concrete. *IOP Conf Ser: Mater Sci Eng* 2020;864:12039.
- [42] Pan Z, Tao Z, Cao YF, Wuhrer R, Murphy T. Compressive strength and microstructure of alkali-activated fly ash/slag binders at high temperature. *Cem Concr Res* 2018;86:9–18.
- [43] Fang H, Visintin P. Structural performance of geopolymer-concrete-filled steel tube members subjected to compression and bending. *J Constr Steel Res* 2022;188:107026.
- [44] Katwal U, Aziz T, Tao Z, Uy B, Rahme D. Tests of circular geopolymer concrete-filled steel columns under ambient and fire conditions. *J Constr Steel Res* 2022;196:107393.
- [45] Zhou Z, Wang T, Hui C, Li J. Seismic performance evaluation of assembled GCFST column-section steel beam frames with geopolymer concrete walls. *Structures* 2020;28:2537–48.

- [46] Ahmad J, Yu T, Hadi MNS. Behavior of GFRP bar reinforced geopolymer concrete filled GFRP tube columns under different loading conditions. *Structures* 2021;33: 1635–44.
- [47] Mazzolani FM. Aluminum alloy structures. 2nd ed. London: E& FN Spon; 1995.
- [48] European Committee for Standardization (EC9). Eurocode 9: Design of aluminium structures. Part 1-1: General structural rules - General structural rules and rules for buildings. BS EN 1999-1-1:2007, CEN:2007. BSI; 2007.
- [49] European Committee for Standardisation (EC4). Eurocode 4: Design of Composite Steel and Concrete Structures. Part 1-1: General Rules and Rules for Buildings. BS EN 1994-1-1: 2004. CEN:2004. BSI; 2004.
- [50] Mrema E, Itoh Y, Kaneko A, Hirohat M. Corrosion of aluminium alloy A6061-T6 members embedded in alkaline materials. *Corros Eng Sci Technol* 2018;53(2): 102–13.
- [51] Ziemian RD. Guide to stability design criteria for metal structures. 6th ed. John Wiley & Sons; 2010.
- [52] EN ISO 6892-1. Metallic materials-Tensile testing-Part 1: Method of test at room temperature. European Committee for Standardization (CEN). Brussels; 2019.
- [53] Ramberg W, Osgood WR. Description of stress-strain curves by three parameters. Vol. Technical. Washington, D.C.: National Advisory Committee for Aeronautics; 1943.
- [54] Hill HN, Clark JW, Brungraber RJ. Design of welded aluminum structures. *J Struct Div, ASCE* 1960;86(6):101–24.
- [55] Luukkonen T, Abdollahnejad Z, Yliniemi J, Kinnunen P, Illikainen M. One-part alkali-activated materials: A review. *Cem Concr Res* 2018;103:21–34.
- [56] Sadique M, Kadhim A, Atherton W, Kot P. Development of new precursors for one-part alkali-activated geopolymer using industrial wastes, In *Sustainable Environmental Geotechnics* (pp. 115–123).
- [57] Gameiro A, Santos AS, Veiga R, Velosa A. Hydration products of lime–metakaolin pastes at ambient temperature with ageing. *Thermochim Acta* 2012;535:36–41.
- [58] Kim MS, Jun Y, Lee C, Oh JE. Use of CaO as an activator for producing a price-competitive non-cement structural binder using ground granulated blast furnace slag. *Cem Concr Res* 2013;54:208–14.
- [59] Medina C, Sáez del Bosque IF, Asensio E, Frías M, Sánchez de Rojas MI. Mineralogy and microstructure of hydrated phases during the pozzolanic reaction in the sanitary ware waste/Ca (OH) 2 system. *J Am Ceram Soc* 2016;99(1):340–8.
- [60] BS Institution 196-3: 2016, Methods of testing cement, Determination of setting times and soundness. 2016. London, England: British Standard Institution (BSI).
- [61] Prakash R. Mechanical properties and flexural performance of geopolymer concrete. *Int Res J Eng Technol* 2017;4(6).
- [62] Han LH. Tests on stub columns of concrete-filled RHS sections. *J Constr Steel Res* 2002;58(3):353–72.
- [63] Liu D, Gho WM, Yuan J. Ultimate capacity of high-strength rectangular concrete-filled steel hollow section stub columns. *J Constr Steel Res* 2003;59(12):1499–515.
- [64] Su MN, Young B, Gardner L. Testing and design of aluminum alloy cross sections in compression. *J Struct Eng ASCE* 2014;140(9):04014047.